Modeling of Transonic Transitional Three-Dimensional Flows for Aerodynamic Applications

Andrey V. Boiko*
Khristianovich Institute of Theoretical and Applied Mechanics, 630090, Novosibirsk, Russia
Kirill V. Demyanko†
Marchuk Institute of Numerical Mathematics, 119333, Moscow, Russia
Stanislav V. Kirilovskiy‡
Khristianovich Institute of Theoretical and Applied Mechanics, 630090, Novosibirsk, Russia
Yuri M. Nechepurenko§
Marchuk Institute of Numerical Mathematics, 119333, Moscow, Russia
and
Tatiana V. Poplavskaya¶
Khristianovich Institute of Theoretical and Applied Mechanics, 630090, Novosibirsk, Russia

The paper describes a technology designed for computing three-dimensional transonic laminar–turbulent flows at various aerodynamic configurations with the use of the general-purpose computational fluid dynamics code ANSYS Fluent and an integrated special module of computing the laminar–turbulent transition position created on the basis of the autonomous software package LOTRAN 3, developed previously by the authors. Within the framework of this technology, computations with a prolate spheroid and engine nacelle are performed for different Mach numbers ($M_\infty = 0.14$–0.7 Reynolds numbers $Re = 2$–10.38×10^6), and angles of attack ($\varphi = -10$ deg to $+10$ deg). New results are obtained on the position of the laminar–turbulent transition in boundary layers in transonic flow regimes, and the problem of the dominating transition mechanism is considered. The results obtained in the present study are demonstrated to be in good agreement with experimental data on the position of the laminar–turbulent transition available in the literature.

Nomenclature

A, B, C, D	=	matrices
a	=	computational domain boundary
b	=	the distance from the boundary-layer edge to the wall
C_f	=	dimensionless skin-friction coefficient
c	=	dimensionless phase velocity
$c_1, c_2, \phi_{\min}, K, \varepsilon$	=	auxiliary constants
l_{tr}	=	the dimensional length of the laminar–turbulent transition region, m
M	=	global Mach number
N_{CF}	=	threshold value of N-factor for the transition onset due to the crossflow vortices
N_c	=	threshold value of N-factor for the transition onset computed with the Mack formula
N_{TS}	=	threshold value of N-factor for the transition onset due to the Tollmien–Schlichting waves
P	=	static pressure, Pa
Re	=	Reynolds number based of the freestream parameters and the reference length of a body
Re_{x^*}	=	transition onset Reynolds number based on the freestream parameters and local x^* coordinate
T	=	temperature, K
Tu	=	freestream degree of turbulence, %
t	=	dimensionless time
U	=	streamwise velocity, m/s
W	=	transverse velocity, m/s
X, Y, Z	=	dimensionless global Cartesian coordinate system
X_1	=	dimensionless turbulization coordinate for the upper airfoil surface
X_2	=	dimensionless turbulization coordinate for the lower airfoil surface
X^*, Y^*, Z^*	=	dimensional global Cartesian coordinate system, m
x, y, z	=	streamwise, wall-normal, and transverse dimensionless coordinates in local coordinate system
x^*	=	streamwise dimensional coordinate in local coordinate system
y_c	=	minimum distance from the wall such that $U(y_c) = c$
α	=	dimensionless streamwise wave number
β	=	dimensionless transverse wave number
δ^*	=	displacement thickness, m
θ	=	azimuthal angle, deg
$\lambda(c), \nu(c)$	=	auxiliary functions
ν	=	kinematic viscosity, s^{-1}
ρ	=	density, kg/m^3
τ_{w}	=	shear stress, Pa
Φ	=	eigenvector
φ	=	angle of attack, deg
ϕ	=	slope of wave vector for crossflow vortices

*Chief Researcher, Department of Aerophysical Studies of Subsonic Flows, Khristianovich Institute of Theoretical and Applied Mechanics, Siberian Branch.

†Senior Researcher, Marchuk Institute of Numerical Mathematics.

‡Researcher, Department of Physics and Problems of Flow Control, Khristianovich Institute of Theoretical and Applied Mechanics, Siberian Branch.

§Leading Researcher, Marchuk Institute of Numerical Mathematics.

¶Leading Researcher, Department of Physics and Problems of Flow Control, Khristianovich Institute of Theoretical and Applied Mechanics, Siberian Branch.

ω	=	dimensionless angular frequency

Subscripts

e	=	at the boundary-layer edge
max	=	maximum value
min	=	minimum value
w	=	at the wall
∞	=	at the inlet boundary of the computational domain

I. Introduction

PROBLEMS of adequate simulation of the laminar–turbulent transition (LTT) are similar to problems of turbulence modeling, but the issues of development and verification of the corresponding models are still much less studied despite comprehensive special investigations in this field (see, e.g., the review in Ref. [1]). Particularly, the ambient flow in cruise flight is characterized by a relatively low degree of turbulence, in contrast to a relatively high degree of turbulence occurring in turbomachinery applications [1]. For engineering purposes, the description of the transition process in boundary-layer flows at low freestream turbulence can be divided into the following spatially consecutive stages: receptivity of the near-wall flow to external disturbances, linear instability of the boundary-layer disturbances, and final breakdown of the flow to turbulence due to nonlinear processes caused by large-amplitude disturbances. Receptivity describes the processes of generation of small-amplitude boundary-layer disturbances by different external and surface perturbations (such as freestream acoustic noise and turbulence, surface vibrations and roughness, etc.). At the next stages, some of the boundary-layer disturbances amplify exponentially in a characteristic direction and initiate the final breakdown.

It is customary to express the boundary-layer disturbances as a set of different waves or modes, which are periodic in space, time, or both [2]. In two-dimensional (2-D) flows, such exponentially growing travelling waves are the Tollmien–Schlichting (TS) waves; also, in high-Mach-number flows, the so-called second or acoustic mode can become dominant. In the case of three-dimensional (3-D) aerodynamic flows with the presence of a crossflow, such as the swept-wing boundary layers or high-angle-of-attack engine nacelle boundary layers, the growing stationary (crossflow, or CF) vortices can be dominant in the transition process. Generally, the transition can be a competition of different instabilities. However, the evolution of such small-amplitude disturbances in all the cases is accurately described by the linear stability theory. Hence, one of the most popular modern approaches to modeling the transition is the use of specialized software, which describes the propagation of small-amplitude boundary-layer disturbances and estimates the transition position using criteria based on threshold disturbance amplitudes indicating the transition onset and breakdown to turbulence. This approach introduced in 1956 in two independent publications [3,4] is now called the e^N-method, which has grown into a branching set of different techniques of determining the characteristic threshold amplitudes (see, e.g., Ref. [5]).

The e^N-method was implemented in several codes used internally by different companies (see, e.g., Refs. [6–11]). The COSAL software [6] is probably one of the earliest black box codes developed for the transition prediction in 3-D compressible boundary layers. However, no integration with external computational fluid dynamics (CFD) software was provided, and only one N-factor strategy was implemented; the desired wave vectors were input manually. Also, to escape the need of finding the disturbance growth direction, the approach was limited by the instability in time; and the integration path was defined by the curve whose tangent is defined by the real part of the group velocity vector. A decade later, the last limitation was removed with the development of the next-generation codes eMalik [7] and GTPT [8]. The LASTRAC software [9] is a further step forward in the application of more advanced transition prediction approaches as the parabolized stability equations (PSEs) coupled with the analysis of flow receptivity to external disturbances, and it accounts for the wall curvature. The STABL software suite with the

PSE-Chem solver of PSE equations [10] is primarily directed to axisymmetric hypersonic boundary layers because it includes chemical nonequilibrium effects. As in the previous approaches, the choice of frequencies and spanwise wave vectors, as well as the dominant mode type, are manual.

As seen, the aforementioned codes have the advantage when used to predict the transition in either axisymmetric or infinite swept-wing cases; moreover, the LASTRAC software can predict with a very high accuracy if proper input data for the receptivity are provided. In contrast, in industrial applications, the focus is frequently shifted to the use of the transition prediction in automatic cycles of shape optimization; in which case, various 3-D geometries and flow directions can occur, combined with a limited knowledge of disturbance flow conditions and surface roughness. To this end, the authors of Ref. [11] supplied necessary accessories to the DLR, German Aerospace Center's (DLR's) local linear stability code LILO and combined it with the proprietary Reynolds-averaged Navier–Stokes (RANS) solver TAU. It was reported that the accessories included the internal boundary-layer code COCO to optionally improve tapered swept-wing flow computations supplied by the RANS solver, as well as some frequency and spanwise wave vector range estimators for TS waves and crossflow vortices. The direction of disturbance propagation can be prescribed either along inviscid flow streamlines or line-in-flight cuts of the geometry to be used with COCO. For the transition prediction an approach based on two different N-factors was used.

However, the e^N-method is still not represented in general-purpose public CFD software products, but it can be implemented by a third-party developer as a plug-in module. Currently, one of the most popular CFD tools for modeling aerodynamic flows is ANSYS Fluent. This product also includes the empirical Transition SST model for the transitional and turbulent flow simulation [12], which is actively used in academic and industrial communities for incompressible flows. However, its application for aerodynamic flows with a relatively low degree of freestream turbulence, particularly for 3-D flows and for flows at high speeds, has some difficulties and limitations (see, e.g., Refs. [1,13]).

In 2013, Boiko et al. [14] and Nechepurenko and Boiko [15] developed from scratch a local transition analysis (known as LOTRAN) software package for computing the transition position in boundary layers of viscous incompressible fluid flows past low-curvature surfaces. Its further development [16] resulted in a new package called LOTRAN 3, designed for the basic academic research of stability of 3-D boundary layers of viscous compressible flows and for determining the transition position by the e^N method. It has an original framework to formulate and solve problems of stability of 3-D boundary layers, to automatically choose ranges of local wave numbers using physical grounds, and to apply filters discarding spurious eigenvalues of different natures.

The present paper describes both the integration of the LOTRAN 3 package into the ANSYS Fluent CFD software with the addition of special software interfaces and unique (to our knowledge) details of the LOTRAN 3 realization directed to make it scalable and reliable in practical applications. To this end, a prototype of the resulting software module was tested in some fundamental scientific and engineering computations (see, e.g., Refs. [17–20]); as a result, many new techniques were added to ensure reliability of operation in essentially different 3-D flows in the Mach number range from approximately 0 to 1.5 with no need of retuning the package parameters. It should be noted that these innovative features distinguish LOTRAN 3 from the other software packages based on the e^N-method but designed either for nonpublic CFD codes or for narrow (in terms of the surface geometry, types of flow instability, and admissible velocity range) classes of flows. In particular, problems of determining automatically the position of the LTT in subsonic and transonic boundary layers on complex-shaped bodies were considered in Refs. [17–20] by using the LOTRAN 3 software package.

The goal of the present study is to demonstrate the ability of the LTT module developed on the basis of the LOTRAN 3 package in conjunction with the ANSYS Fluent software system to predict automatically the LTT position on some typical bodies (flat plate,

airfoil, prolate spheroid, engine nacelle) including transonic flows. This means that all computations can be performed without retuning critical package parameters for a particular flow. Specific features of modeling the base flow with accuracy acceptable for practice and using the LTT module for computing the LTT position in transonic boundary layers are also considered. To validate the developed computational technology, the predicted results on the LTT position are compared with available experimental data reported in the literature.

It should be noted that LTT in transonic 3-D boundary layers of different elements of flying vehicles is extremely important for designing advanced-technology aircraft, but it has still been insufficiently investigated. The majority of corresponding studies is limited to a consideration of swept-wing flows (see, e.g., Refs. [21–23]). Meanwhile, data on the position and possible dominating mechanisms of the LTT in a transonic flow with a low degree of freestream turbulence necessary for the development of a laminarized engine nacelle for reducing the friction drag on its external surface can hardly be found in the literature, except for two-dimensional cases [24]. Therefore, for 3-D configurations, the dominating mechanisms of the LTT in the boundary layer on a body placed at an angle of attack in a transonic gas flow are also discussed.

II. Base-Flow Simulation

A laminar boundary layer (base flow) formed in subsonic and transonic streams at various configurations with low degrees of freestream turbulence ($Tu < 1\%$) was numerically simulated by the ANSYS Fluent software. The data obtained on the base flow were transferred to the LTT module for determining the LTT position. The authors' gained experience in computing laminar–turbulent flows at various bodies with the use of ANSYS Fluent together with the LTT module made it possible to formulate the following approach to base-flow modeling:

1) Generate a computational grid around the examined surface with an allocated near-wall layer of height significantly exceeding the characteristic thickness of the laminar boundary layer with enough cells for a proper resolution of the boundary layer.

2) Generate a regular hexahedral (quadrangular in 2-D computations) fine computational grid in the allocated region with further refinement toward the surface (a hexahedral grid with longitudinal edges of the cells almost parallel to the streamlines along the body is the most effective grid from the viewpoint of computational efficiency [25]).

3) Compute the laminar base flow with the RANS equations. Note, that in the case of appearance of unsteady laminar flow separation, the steady computation of the base flow fails. In this case a preliminary splitting of the flow domain into the laminar and definitely turbulent (including the major part of the separated flow) regions is performed to remove the unsteadiness and obtain the required converged solution.

In the present study, we consider four different configurations: a 3-m-long flat plate with a blunted leading edge (with the rounding radius of 0.3 mm) [17]; a supercritical NASA-SR-0410 airfoil with a chord length of 0.2 m [26]; a prolate spheroid with a length of 2.4 m, a diameter of 0.4 m, and a ratio of semiaxes equal to 6:1 [27–29]; and a ducted engine nacelle. The contour of the engine nacelle provided a sufficiently long region of the laminar and transitional boundary layer. The engine nacelle was designed by means of rotating this contour around the longitudinal axis by 180 deg; i.e., it was an axisymmetric (with respect to the longitudinal axis) ducted body of revolution. The length of the engine nacelle was 0.6 m.

Figure 1 shows fragments of the computational grids. The flow past a flat plate was computed on a regular rectangular grid (Fig. 1a) refined toward both the surface of interest and the leading edge. The computational area consisted of a rectangle and a quarter-circle with a radius of 7 m, with the flat plate placed in the center of the lower boundary (Fig. 1a). The distance from the trailing edge of the plate to the outlet boundary along the x axis was also 7 m. The computational area for the flow around the airfoil also consisted of a rectangle and a quarter-circle. The airfoil was located in the center, and the outer boundary of the computational area was moved away at a distance of more than 10 chord lengths, i.e., ≥ 2 m. In the airfoil computations,
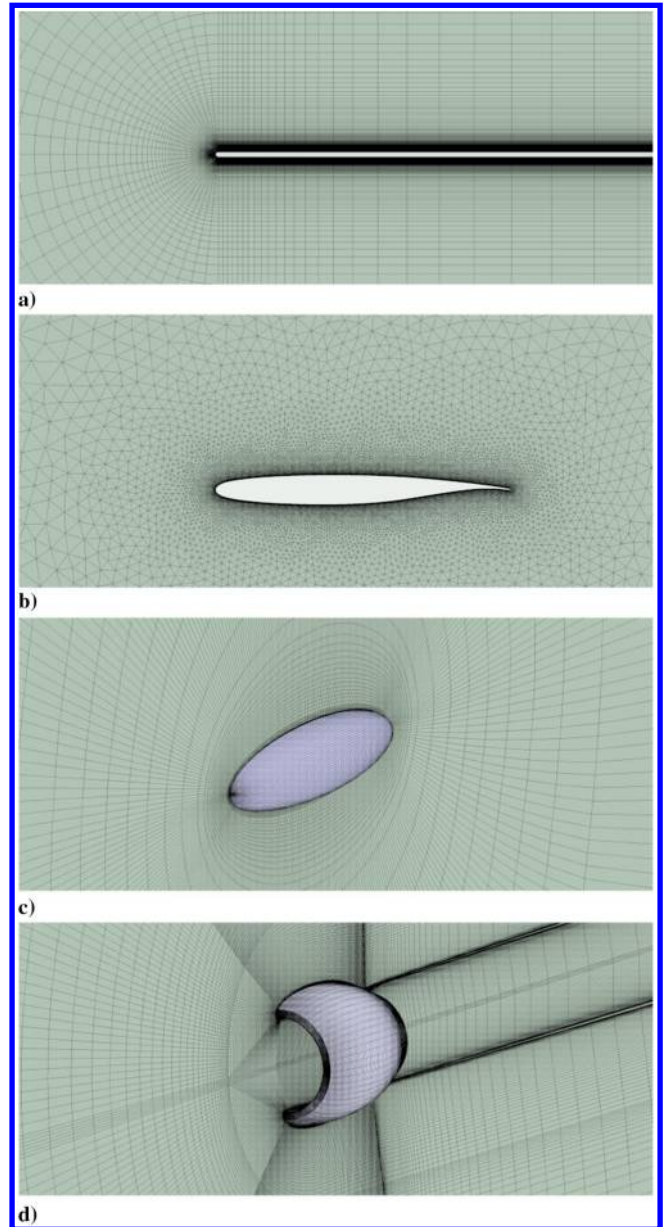

Fig. 1   Fragments of computational grids: a) **near the leading edge of the flat plate;** b) **near the airfoil (each fourth cell); and c,d) in the plane of symmetry of the prolate spheroid and engine nacelle, respectively (every eighth cell).**

the allocated near-wall region was covered by a regular rectangular grid refined toward the surface, whereas the remaining computational domain was covered by an irregular triangular grid (Fig. 1b). For 3-D bodies (the prolate spheroid and engine nacelle), for the prolate spheroid, the computational area consisted of a hemisphere with a 6 m radius. For the engine nacelle, the computation area consisted of a hemisphere with a 10 m radius joined with a cylinder with a 10 m radius and length. A regular hexahedral grid was generated at the wall for the prolate spheroid and the engine nacelle (Figs. 1c and 1d, respectively); and the height of the near-wall region was five times the boundary-layer thickness or more. It should be noted that the LTT module received data on the grid structure and flow parameters only from the allocated near-wall region to make the data analysis less time-consuming.

For the prolate spheroid, the computational grid in the allocated near-wall region with a 40 mm height had 160 cells in the normal-to-wall direction, with approximately 80 of them covering the boundary-layer region. In the case with the engine nacelle, the near-wall region height was 10 mm, and the grid contained 50 cells in the normal-to-wall direction, with approximately 35 of them

covering the boundary-layer region of interest. In both cases, each cell corresponded to approximately 2 deg in the azimuthal direction. In the streamwise direction, there were 612 and 204 cells for the prolate spheroid and engine nacelle, respectively. Thus, the total number of cells in the computational domain was 18 million for the prolate spheroid and 7 million for the engine nacelle. Computations on a sequence of nested grids (with a twofold increase of the number of cells in each of the x and y directions and with a 1.2-fold increase in the z direction) showed that the difference in the results on the LTT onset was within 2% (here and in the following, the accuracy of the transition position is scaled by the length of the body of interest).

A density-based solver for the governing equations and an implicit scheme with the second order of accuracy in space with the Roe–Flux-Difference-Splitting method. The freestream conditions at the external boundary of the computational domain were the pressure P_∞, Mach number M_∞, temperature T_∞, and angle of attack φ; the surfaces were subjected to the no-slip conditions and the constant wall temperature for the 2-D configurations, as well as the adiabatic wall conditions for the 3-D configurations. The global Cartesian coordinate system (X^*, Y^*, Z^*) was applied. The X^* axis coincided with the axis of symmetry of all bodies under consideration, except the airfoil, in which case X^* axis is directed along the wing chord. The origin of the global Cartesian coordinate system was located at the center of the circle of leading-edge bluntness for the flat plate, at the tip for the airfoil, at the geometric center of the prolate spheroid, and at the point of intersection of the axis of symmetry with the plane of the leading edge for the engine nacelle. Later in the paper, the dimensional coordinates are scaled by the length of the corresponding body; and dimensionless variables X, Y, and Z are used. The Reynolds number Re is computed on the basis of the freestream parameters and the dimensional length of the corresponding body.

As has already been noted earlier in this paper, a region of laminar separation may occur in the flow simulations, leading to oscillations of the solution in this region, which deteriorates the convergence. These oscillations may distort the upstream laminar boundary layer, whose stability is to be studied. To minimize these oscillations, the base flow was computed with the use of a turbulence model that includes turbulent viscosity with preliminary splitting of the flow domain into the laminar and definitely turbulent parts (the latter includes the major part of the region of unsteadiness). The position of initial turbulization was estimated in preliminary computations of the laminar flow based on the place where the oscillations associated with the flow separation appeared (for the flat-plate case, the initial turbulization was not used). For example, Fig. 2 shows the distributions of the skin-friction coefficient $C_f = \tau_w/(0.5\rho_\infty U_\infty^2)$ (τ_w is the wall shear stress, U_∞ is the freestream velocity, and ρ_∞ is the freestream fluid density) over the upper surface of the airfoil, which was obtained in computations of the laminar flow regime and the flow regime with nonzero turbulent viscosity beginning from a certain prescribed value of the streamwise coordinate. The values of $C_f = 0$ refer to the laminar separation region. It is seen that the value of C_f decreases to zero at $X \approx 0.75$. The field of the streamwise velocity derivative with respect to the streamwise coordinate shows that flow oscillations appear on the upper
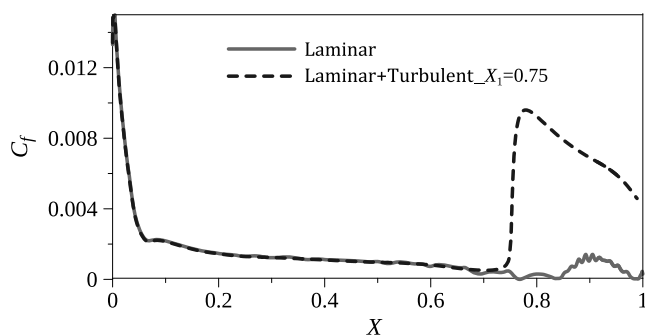
surface of the airfoil at $X = 0.75$. They are manifested as the alternation of regions of flow acceleration and deceleration. A similar behavior is observed on the lower surface at $X \approx 0.5$. These two values are taken as the turbulization coordinates $X_1 = 0.75$ and $X_2 = 0.5$ for the upper and lower airfoil surfaces, respectively. The turbulization positions are imposed by a specially developed ANSYS Fluent user-defined function (UDF) module.

Two methods of flow turbulization were used in the present study. In the first method used in 2-D computations, the UDF module was applied to change the turbulent viscosity in the Spalart–Allmaras turbulence model so that it was equal to zero in the laminar region before the turbulization coordinate X_1, and then it was computed in the usual (unchanged) way implied in the model. In the second method used in 3-D computations, the computations were performed with the k-ω-SST turbulence model; and the turbulent kinetic energy k was assumed to be equal to zero before the turbulization coordinate at each time step (with the help of the UDF module). As a result, there was a laminar flow upstream of X_1, followed by natural growth of the turbulent kinetic energy downstream of X_1, which makes the transition from the laminar to turbulent flow smoother. On this basis, an intermittency field is constructed. In the laminar and the turbulent flow regions, the intermittency equals zero and one, respectively. The distributions of the skin-friction coefficient C_f on the body surface in the cases with nonzero turbulent viscosity are also shown in Fig. 2.

At the next stage, the computational grid and base-flow data computed in the allocated near-wall region are transferred to the LTT module.

III. Transition Prediction Method

In the LOTRAN 3 software package, the evolution of small perturbations in the boundary layer is described by full equations of heat and mass transfer of a compressible medium linearized with respect to the laminar base flow [16]. Therefore, the package can be used for a wide range of speed values, including for high-speed base flows, but this paper describes only the specific features of LOTRAN 3 application to subsonic and transonic streams.

The LOTRAN 3 software package has a modular structure (see Fig. 3) with the separation of problems of computational 3-D geometry, base-flow data analysis and assimilation, stability analysis, and prediction of the LTT position on the basis of the stability analysis and data on factors initiating flow turbulization. Note that in contrast to the other transition prediction software discussed in the Introduction (Sec. I), no boundary-layer code to "improve" the CFD data is included. The computations are completely automated. The package operates with base-flow data obtained with engineering accuracy. In analyzing the stability, the majority of the computations are performed by standard, carefully approved matrix algorithms. It is also possible to visualize various characteristics of the boundary layer
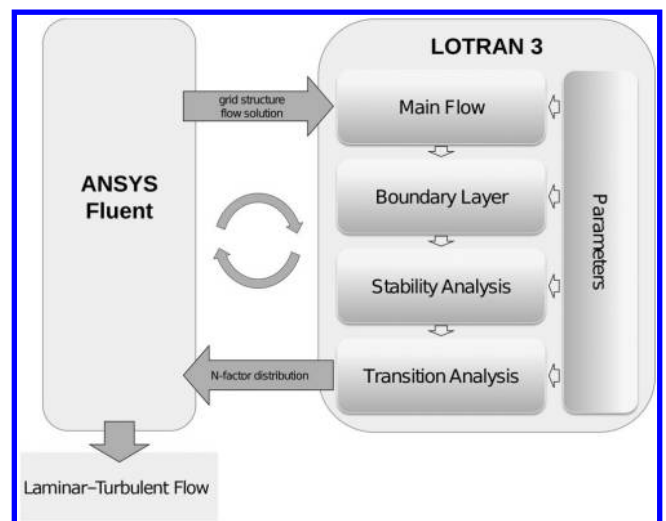

Fig. 2 Distributions of the skin-friction coefficient on the upper surface of the airfoil: $Re = 10^6$, $\varphi = 0$, $M_\infty = 0.25$, $T_\infty = 296$ K, and $T_w = 300$ K.

Fig. 3 Structure of the LOTRAN 3 software package.

and the results of its stability analysis. The main result of operation of this package is the distribution of N factors of the growth rates of disturbances on the surface of interest. A typical result is shown in Fig. 4 for the prolate spheroid at an angle of attack of 10 deg to the freestream. The LTT position is found from the distribution of N factors by the e^N method on the basis of data on threshold N factors.

The values of parameters controlling the computations are set in the Parameters need a different font module. In the course of the computations, they are passed to all other modules. The results reported in Sec. IV were obtained for a single set of parameters to demonstrate the software versatility. However, it is possible (but not obligatory) to tune some parameters for a class of configurations to accelerate computations without compromising the final accuracy.

The MainFlow need a different font module reads the computed data on the base flow and converts them to an internal representation of the LOTRAN 3 package. Namely, the data are mapped onto a nonconformal tetrahedral grid with the velocity components, temperature, and pressure being defined at the vertices of this grid and with the intermittency coefficient being specified at the surface vertices. To reduce the computational expenses of 3-D geometry manipulations, a special structure is generated on the set of tetrahedrons by means of space splitting into identical boxes in the Cartesian or cylindrical coordinate system. This is the only module that depends on the grid used, the method of data setting, and the approximation in laminar flow computations.

The BoundaryLayer module operates with the data on the base flow in the internal representation. It forms 2-D nonplanar slices of the boundary layer along the prescribed lines of disturbance propagation. There are several approaches to select the lines with, e.g., the direction of group velocity [30] or line-in-flight cuts [11]. In practice, in accordance with experimental evidence and numerical observations (see, e.g., Refs. [11,31–35]), these lines are close to or coincide with the real streamlines close to the boundary-layer edge in the region of interest or with the so-called boundary-layer edge streamlines, which have a simple physical interpretation as surface streamlines in the inviscid approximation [11,36].

Two algorithms for computing such slices are implemented in the module. In both algorithms, the surface tetrahedron is chosen, and the external normal to the surface is drawn from the barycenter of the tetrahedron base; a grid is constructed on this normal (with

refinement toward the surface) and data on the base flow are interpolated to this grid. Then, these data are processed by a separate utility. In the utility, based on the enthalpy distribution analysis (Bernoulli's equation for compressible flows), the location of the boundary-layer edge is estimated and a local (associated with the normal) orthonormal basis is constructed. Note that, using the Bernoulli equation, we implicitly assume that the enthalpy is constant along the inviscid streamline, which is reasonable in the case of subsonic and transonic flows of interest. The direction along the normal is chosen as the local vertical direction, the component of the velocity vector at the boundary-layer edge perpendicular to the normal is taken as the streamwise direction, and the direction orthogonal to the first two directions and forming the right-hand coordinate system with them is considered as the transverse direction. The data in grid nodes are presented in the local basis. In this case, x is the streamwise coordinate (length of the arc along the surface from the beginning of the 2-D slice, which will be constructed, to the base of the normal), y is the vertical coordinate (distance to the surface along the normal), and z is the transverse coordinate. Then, it is checked whether the chosen normal lies in the region of the formed attached boundary layer. For this purpose, it is verified that the intermittency coefficient at the base of the normal is smaller than the threshold value, that there is no separation, and that the maximum absolute value of the vertical component of velocity inside the boundary layer is significantly smaller than the streamwise component of velocity at the estimated boundary-layer edge. If the chosen normal does not satisfy at least one of these criteria (i.e., it is not located in the formed attached boundary layer), then a new surface tetrahedron located slightly upstream is automatically chosen, the external normal to the surface is drawn from the barycenter of this tetrahedron, etc. When the normal in the region of the formed attached boundary layer is found, the initial point on this normal is chosen at a distance from the surface proportional to the boundary-layer thickness.

In the first algorithm for constructing the 2-D slice, the streamline upstream and downstream from the chosen initial point is computed by solving the corresponding system of ordinary differential equations by the fourth- or fifth-order Runge–Kutta method. The required base-flow velocity in the nodes of numerical integration is interpolated from the nonconformal tetrahedral grid. Then, the 2-D slice of the boundary layer is constructed along the resultant streamline: a
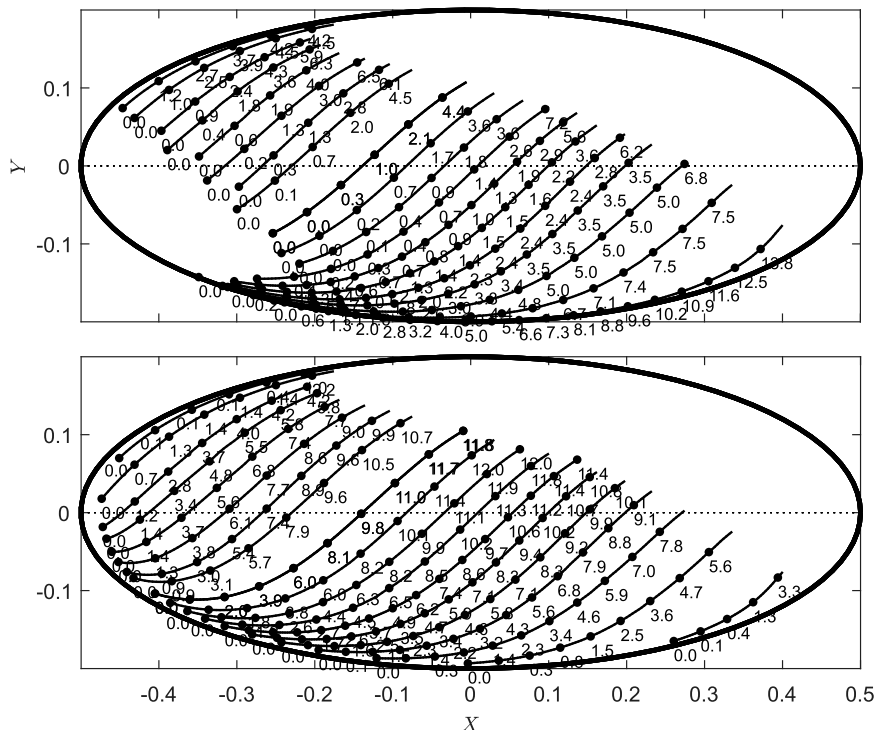

Fig. 4 Distributions of the N-factors over the prolate spheroid surface along the streamline projections for the a) TS waves, and b) CF vortices. $Re = 7.2 \times 10^6, \varphi = 10 \ \text{deg}, M_\infty = 0.7, \text{and Tu} = 0.2\%.$

uniform grid is chosen on the streamline, a normal is drawn from each node of the grid onto the surface, a grid similar to that generated on the initial normal is constructed on this normal, and the base-flow parameters are interpolated onto this grid. Based on the enthalpy distribution analysis, the boundary-layer edge is determined, and a local orthonormal basis is constructed. The data at the grid nodes are presented in the local basis.

A normal located downstream from the initial normal is rejected if it does not lie in the region of the formed attached boundary layer, and all normals located further downstream are rejected as well. If the first two criteria of the formed attached boundary layer are satisfied but the third one is not for a normal located upstream from the initial one, then the 2-D slice is rejected. If the first criterion is satisfied but the second one is not, then the whole 2-D slice is rejected and a new initial normal is selected upstream. Moreover, if the distance between two adjacent normal bases is smaller than a given threshold value, one of such normals is also rejected. The corresponding threshold values are defined in the Parameters module.

Note that if the first two criteria are satisfied, then the third criterion may not be met only near the leading edge if the normals to the surface (due to the surface curvature) have small angles with the freestream velocity vector. In the latter case, the vertical velocity component is comparable or even greater than the streamwise one (in the local basis). Thus, if some normal located upstream from the initial one is rejected by the third criterion, we can reject the normals located further upstream.

In the second algorithm, the velocity vector projection onto the surface is computed for the chosen initial point on the initial normal. A step up to the surface edge is made in the plane of the base of the initial tetrahedron in the direction of the projection. From the resultant point on this surface edge, the external normal is drawn to the base of another surface tetrahedron for which this edge is common with the initial tetrahedron. The procedure is continued while the next normal is located in the formed attached boundary layer. Thus, a 2-D slice in the downstream direction is constructed. To construct the slice in the upstream direction, the direction of motion is chosen to be opposite to the velocity vector projection onto the surface.

It should be noted that the first algorithm is less expensive and is used as a default. The second algorithm is better approved by laboratory investigations [37] and is used if higher accuracy is needed or results obtained by the first algorithm have to be verified. In the examined 3-D flows, the slices constructed by these algorithms are very close.

The characteristic values of the maximum streamwise wave number of the TS waves, the maximum absolute value of the transverse wave number of CF vortices, and the cotangent of the slope of their wave vector are computed for each normal. The order of magnitude of the maximum value of the streamwise wave number of the neutral TS waves is estimated by the following formula [38]:

$$\alpha_{\max} \approx U'_w c_{\max} \sqrt{1 - M^2(1 - c_{\max})^2}$$

Here, the prime means the derivative with respect to y, U'_w is the derivative of the streamwise component of velocity at the surface, M is the Mach number, and $c_{\max}$ is the maximum phase velocity c of the neutral TS waves (for this formula, local scaling on corresponding values at the boundary-layer edge was used). The value of $c_{\max}$ can be estimated using the modified Tietjens function, which appears when the linearized equations of heat and mass transfer are transforming by the method of successive approximations [38]. Particularly, $c_{\max}$ occurs when the imaginary part of the modified Tietjens function reaches its maximum value of about 0.58; in which case, the eigenvalue problem to find the neutral TS wave phase velocity is reduced to the nonlinear equation:

$$[1-2\lambda(c)]v(c) \approx 0.58$$

where

$$v(c) = -\pi \frac{U'_w c}{T_w} \left[\frac{T^2}{(U')^3} \left(\frac{U'}{T} \right)' \right]_{y=y_c}, \lambda(c) = \frac{U'_w y_c}{c} - 1$$

are auxiliary relations presented in this form to underline significant roles of the wall temperature and wall shear stress ($\sim U'_w$), as well as of the position of the critical layer. Here, y_c is the coordinate of the critical layer that is the minimum distance from the wall such that $U(y_c) = c$, and T is the temperature.

For CF vortices, the characteristic values of the maximum absolute values of the transverse wave number β and the cotangent of the slope of the wave vector are estimated by the formulas [39]

$$|\beta| = \frac{1}{y}, \cot(\phi) = -\frac{W(y)}{U(y)} \tag{1}$$

where y is the solution of the equation

$$\frac{d^2 \rho W}{dy^2}(y) = 0, d \leq y \leq b$$

Here, b is the distance from the wall to the boundary-layer edge, W is the transverse component of velocity, d is the position of the maximum of its absolute values, and $\rho(y)$ is the base-flow density. Both estimations follow from considering the CF neutral disturbances in the inviscid limit. The first expression is rather empiric, whereas the second gives a direction, which is very close to the direction of propagation of the stationary CF neutral disturbances. Recall that in the inviscid limit, the velocity profile along this direction has an inflection point at the wall (see, e.g., Ref. [40] for details).

The StabilityAnalysis module is used to investigate the local stability of the boundary layer to the TS waves and CF vortices on the normals to the surface along the constructed 2-D slices based on the full equations of heat and mass transfer linearized with respect to the base flow. Each of these problems implies consideration of the local stability to disturbances of the form

$$g(x, y, z, t) = \tilde{g}(y)e^{i(\alpha x + \beta z - \omega t)}$$

where t, α, β, and ω are the time, the streamwise wave number, the transverse wave number, and the angular frequency, respectively. Substitution of the disturbance of this form into the full equations of heat and mass transfer for a compressible medium linearized with respect to the base flow (see, e.g., Ref. [41]) and spatial approximation of the resultant system of equations lead to eigenvalue problems of the form with matrices A, B, C, and D depending on the streamwise variable through the base-flow profiles of the velocity, temperature, and pressure, as well as the transverse wave number [16]. Generally, disturbances with different spanwise wave numbers and frequencies should be considered. However, in subsonic and transonic flows, the TS waves with a zero transverse wave number [41] and the stationary CF vortices at a low freestream degree of turbulence specific for aerodynamic applications are usually dominant disturbances [42]. Hence, in the following computations, a zero value is set for the transverse wave number in the case of the TS waves and for the angular frequency in the case of CF vortices (in a real-life situation, special checks for the validity of these assumptions are desirable). In both cases, the boundaries of instability regions are first estimated, and then the growth rates of disturbances in the downstream direction in these instability regions are computed by means of solving spatial eigenvalue problems.

The boundaries of the instability region for the TS waves are estimated by solving temporal eigenvalue problems (using the QR algorithm), i.e., eigenvalue problems with respect to the complex angular frequency for a specified real value of the streamwise wave number. The neutral curve is computed. Then, for each point of the beginning of the instability region, the downstream evolution of the spatial growth rate of the corresponding TS wave is computed.
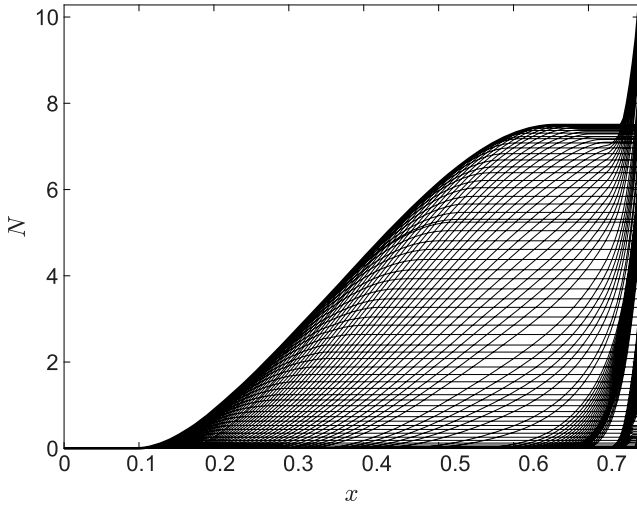
Fig. 5 _N_-factors of the TS waves in the instability regions: prolate spheroid, $Re = 7.2 \times 10^6$, $\varphi = 10$ deg, and $M_\infty = 0.7$.

The order of magnitude of the maximum value of the streamwise wave number, at which the temporal eigenvalue problems are solved, is estimated as the mean (on the 2-D slice considered) value of $\alpha_{\max}$ computed at the last stage of the 2-D slice construction. After solving each eigenvalue problem, the eigenvalues corresponding to the TS waves are chosen from the whole eigenspectrum by using a filter limiting the admissible range of the phase velocity of $c = \text{Real}(\omega)/\alpha$. The experience of computing various configurations shows that it is sufficient to use the domain $0.3 \leq c \leq 0.6$ for subsonic and transonic flows.

In the case of CF vortices, the instability region boundaries are estimated by solving partially parabolized (with the term $-\alpha^2 A$ being rejected) spatial eigenvalue problems (using the QR algorithm), i.e., the eigenvalue problems with respect to the complex streamwise wave number for a specified real value of the transverse wave number and zero frequency. The neutral curve is computed. Then, the downstream evolution of the growth rate of the transverse vortex for each onset of the instability region is computed by solving the original (not parabolized) spatial eigenvalue problems.

For every constructed 2-D slice the maximum absolute value of the transverse wave number to be considered is estimated as the mean value of $|\beta|$, where β is computed with Eq. (1). The eigenvalue α corresponding to CF vortices with a fixed value of β are selected after solving the eigenvalue problems using the following restrictions on α:

Fig. 6 _N_-factors of CF vortices in the instability regions: prolate spheroid, $Re = 7.2 \times 10^6$, $\varphi = 10$ deg, and $M_\infty = 0.7$.

$$c_1 |\cot(\phi)| \leq \left|\text{Real}\left(\frac{\alpha}{\beta}\right)\right| \leq \min\{\cot(\phi_{\min}), c_2 |\cot(\phi)|\}$$

for selecting the range of propagation directions specific for the growing CF vortices,

$$\text{Real}\,\alpha > 0$$

for selecting disturbances with the positive streamwise wave number only,

$$-\text{Imag}\,\alpha \leq K$$

for removing the continuous spectrum in the lower half-plane, and the following restrictions on the streamwise velocity component u of the corresponding eigenvector:

$$\|u\|_{[b,a]}/\|u\|_{[0,a]} \leq \varepsilon$$

which ensures that the disturbance maximum is located inside the boundary layer and effectively rejects occasional spurious modes. Here, a is the distance from the wall to the computational domain boundary (corresponding to the far-field edge).

The empirical constants c_1, c_2, $\phi_{\min}$, K, and ε used in the filters are chosen on the basis of the previous experience; the default values are 0.25, 2, $\pi/3$, 50, and 0.2.

Finally, the N-factors are computed in the StabilityAnalysis module with the use of computed growth rates along the 2-D slices (Figs. 5 and 6). For each 2-D slice, the envelope is constructed in the TransitionAnalysis module of the N-factors of individual disturbances computed along the slice. In addition, the dimensional length of the LTT region is estimated for each normal. This length is estimated by the formula

$$l_{\text{tr}} = 2.3 \sqrt{\frac{U_e \delta^*}{\nu_\infty}} \delta^*$$

which (taking into account our scaling) is derived from the formula of Ref. [43] for the transition-length Reynolds number. Here, U_e and δ^* are the streamwise components of the velocity at the boundary-layer edge and the displacement thickness on the normal considered, respectively; and ν_∞ is the freestream kinematic viscosity. Then, a file is formed, which contains (among other information) the global Cartesian coordinates of the bases of the normals of all 2-D slices and the corresponding distributions of the N-factors. Based on this information, the user can determine the onsets of the LTT and turbulent regions in each slice by applying prescribed threshold values of the N-factor, and thus determine the LTT region.

IV. Results and Discussion

An application of the introduced approach is demonstrated in the following by four typical aerodynamic configurations. For validation of the developed method of LTT computations, comparisons with data obtained for subsonic and transonic boundary layers were performed.

Figure 7 shows the Reynolds numbers of the LTT onset Re as functions of the Mach number for all four configurations (see Sec. II) at a zero angle of attack with the use of the threshold N factor of the transition onset for the TS waves N_{TS} computed by the Mack formula [44], which with our definition of Tu takes the form

$$N_c = -8.43 - 2.4 \cdot \ln(\text{Tu}/100) \qquad (2)$$

As the Mach number increases while the unit Reynolds number remains constant, the LTT onset is shifted downstream for all four configurations. These data are consistent with the theoretical predictions of the influence of the Mach number on the transition Reynolds number reported in Ref. [45], where it was shown that the transition Reynolds number in the boundary layer on a flat plate increases as the Mach number increases from zero to one. The experimental data on
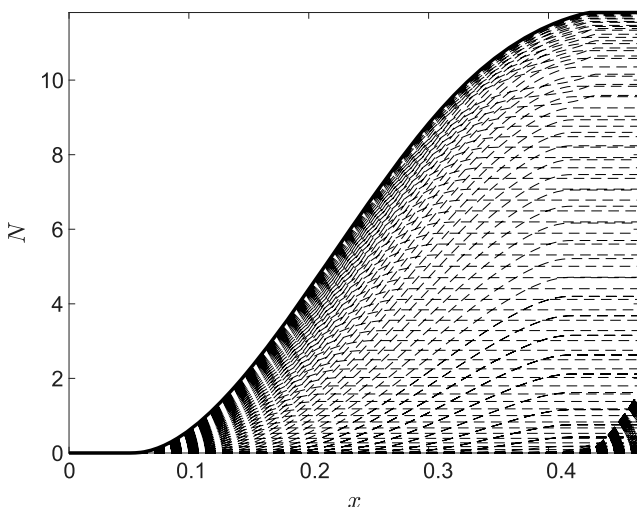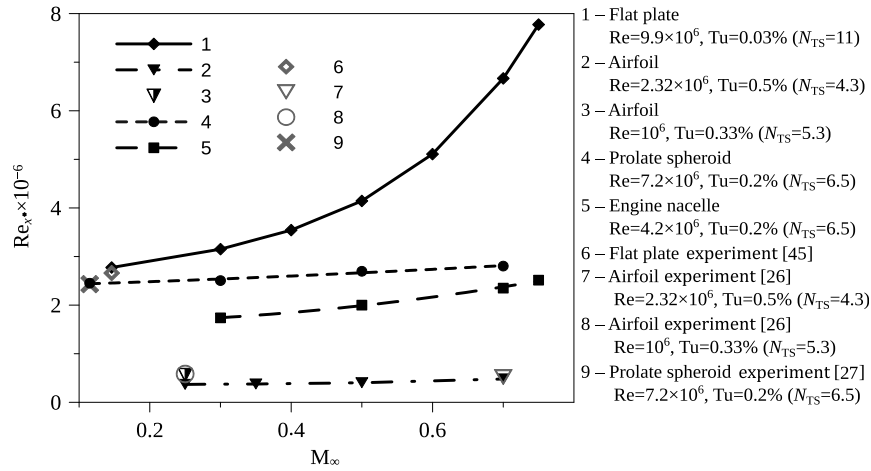
1 – Flat plate
$Re=9.9\times10^6$, Tu=0.03% (N_{TS}=11)
2 – Airfoil
$Re=2.32\times10^6$, Tu=0.5% (N_{TS}=4.3)
3 – Airfoil
$Re=10^6$, Tu=0.33% (N_{TS}=5.3)
4 – Prolate spheroid
$Re=7.2\times10^6$, Tu=0.2% (N_{TS}=6.5)
5 – Engine nacelle
$Re=4.2\times10^6$, Tu=0.2% (N_{TS}=6.5)
6 – Flat plate experiment [45]
7 – Airfoil experiment [26]
$Re=2.32\times10^6$, Tu=0.5% (N_{TS}=4.3)
8 – Airfoil experiment [26]
$Re=10^6$, Tu=0.33% (N_{TS}=5.3)
9 – Prolate spheroid experiment [27]
$Re=7.2\times10^6$, Tu=0.2% (N_{TS}=6.5)

Fig. 7 Reynolds number of the LTT onset versus the Mach number for $\varphi=0$: curves 1–5 show the results computed in the present study; and symbols denoted 6–9 are the experimental data

the LTT position in Fig. 7 (where available) are in good agreement with the results of the present simulations.

A. Compressible Flow at the Prolate Spheroid

The computed LTT lines for a completely 3-D flow at a prolate spheroid [27] are compared in the following with experiments and computations of other researchers. Depending on the freestream conditions, the LTT on this body can be induced by either the TS instability waves or the CF instability vortices, or both. Several test cases from Ref. [27] were chosen: $Re=7.2\times10^6$, $M_\infty=0.13$, $\varphi=0$ and $\varphi=10$ deg, and Tu = 0.1–0.2%. At $\varphi=0$, the LTT is initiated only by the TS instability waves. For this case, the results of the present simulations are compared with the experimental data [27] in Fig. 8, where the laminar, transitional, and turbulent regions of the flow on the spheroid surface at a zero angle of attack are shown. The N factors of the transition onset (8.2) and the turbulence onset (11.2) were selected in accordance with the corresponding experimental data. Note that that the grid used to compute the main flow was symmetrical. However, to compute the transition position, the data from this grid are mapped in LOTRAN 3 onto an unstructured tetrahedral grid, which is not symmetric; hence, the constructed 2-D slices and the data on them are not completely symmetrical as well. This explains some variations of the computed transition positions (within 1.5% of the body length) in the azimuthal direction.

The quantitative results of experiments and computations are compared in Fig. 9 for the prolate spheroid at $Re=7.2\times10^6$, $M_\infty=0.13$, and $\varphi=10$ deg. The comparisons are performed with the experimental data obtained in the F1 wind tunnel of ONERA [46,47] and the DLR 3 m low-speed wind tunnel in Göttingen [26,47], as well as with the numerical data computed for this regime by Stock [47], Krimmelbein and Krumbein [11], Krimmelbein et al. [48], and Krimmelbein and Radespiel [49] using the e^N method. It is seen that all data are in good agreement on the side surface of the spheroid. On the lower surface, there are some differences between the numerical and experimental data, which do not exceed 9%.

A specific feature of the transition process under consideration is an interaction of the TS waves and CF vortices affecting the transition position [47]. As a result, on the larger part of the side surface of the body, the critical N factors depend on the relative amplitudes of both disturbances. This, however, is not an obstacle for application of the e^N method if the stability diagram for the flow, which relates TS and CF N factors, is known. Particularly, such stability diagrams were presented in Ref. [47] for two low-speed subsonic wind tunnels (for which the DLR and ONERA stability diagrams hold) for a set of different angles of attacks and Reynolds numbers based on a large number of experimental studies. The LTT predictions obtained by various researchers using the e^N method with these diagrams, including the present simulations, are all in good agreement.
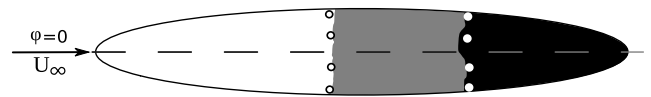

Fig. 8 LTT regions on the prolate spheroid, with $Re=7.2\times10^6$, $M_\infty=0.13$, and $\varphi=0$: laminar (white), transitional (gray), and turbulent (black) regions of the flow. ○ denote experimental data [27] on the LTT and turbulence onsets.
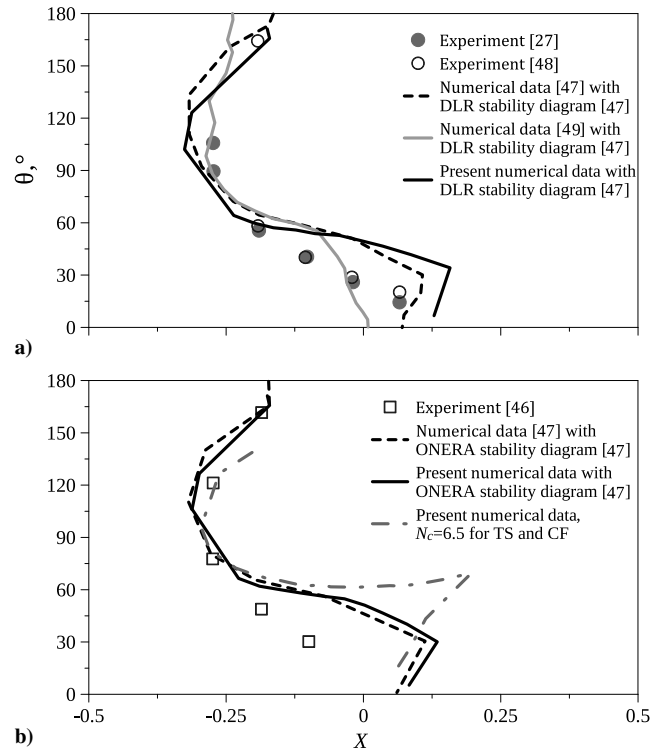

a)

b)

Fig. 9 Positions of the LTT onset versus the azimuthal angle θ in the boundary layer on the prolate spheroid, with $Re=7.2\times10^6$, $M_\infty=0.13$, and $\varphi=10$ deg.

However, there are no such diagrams for transonic flows because of the lack of the corresponding experiments. Therefore, for the present test conditions ($Re=7.2\times10^6$, $M_\infty=0.13$, and $\varphi=10$ deg), we also demonstrate the LTT positions in the boundary layer on the prolate spheroid computed with identical threshold values of both N factors computed by formula (2) for the degree of freestream turbulence of Tu = 0.2% indicated in Ref. [27] (see

Fig. 9b). As seen, the transition to turbulence in this flow regime is caused by the mutual influence of the TS waves and CF vortices only near the lower surface (35 deg $\leq \theta \leq$ 60 deg), whereas CF vortices are mainly responsible for the transition on the side surface (60 deg $< \theta <$ 160 deg). Close to the leeward surface of the prolate spheroid, the LTT is initiated by a 3-D separation of the boundary layer. Hence, the difference from the data computed with the use of the stability diagram is observed in a quite narrow region 35 deg $\leq \theta \leq$ 60 deg, where the evolution of the TS waves was probably affected to a large extent by nonlinear steady CF vortices modulating the base flow [50,51]. On the remaining surface of the prolate spheroid, the present predictions agree well with the other results plotted in Fig. 9. It should be noted that the use of independent N factors for the TS waves and CF vortices implicitly implies weak interaction between these types of disturbances [52,53], which may be considered as the initial approximation to be used in the transonic regimes due to the lack of more detailed calibration data.

Figures 10 and 11 show the results for $M_\infty = 0.7$ (that is, at the lower bound of transonic regimes in aerodynamic applications; however, no local supersonic region was observed in the present case) and different angles of attack as projections of streamlines onto the surface. The same threshold N factors of the transition onset for the TS waves N_{TS} and the CF vortices N_{CF} computed by formula (2) with a corresponding degree of freestream turbulence Tu were used. The black solid curve illustrates a construction of the line of LTT
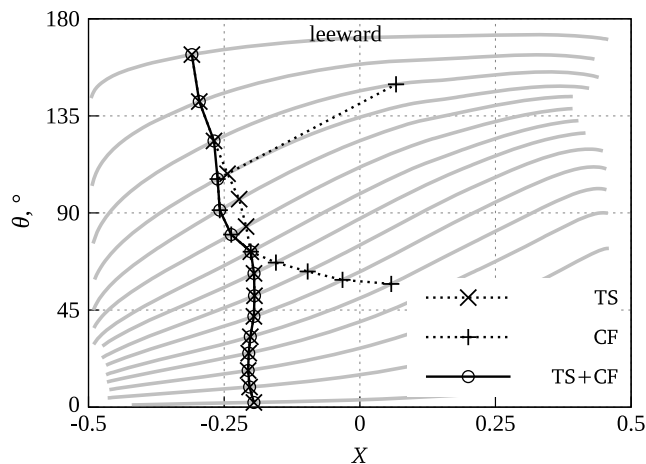
onset in accordance with the threshold value of the N factors computed by Mack formula (2) for Tu = 1%.

In the case with a zero angle of attack, the LTT is initiated by the TS instability waves. In the case of a nonzero angle of attack, the LTT is induced by the combined effect of the TS waves and CF vortices (Figs. 10 and 11). At $\varphi = 5$ deg, the TS instability waves still dominate despite the presence of instability regions of both transition mechanisms. At the angle of attack of $\varphi = 10$ deg, the LTT is induced by the TS waves only near the windward and leeward surfaces, whereas the CF instability dominates on the remaining part of the flow. Thus, as the angle of attack increases, the role of the CF instability becomes constitutive for the prolate spheroid in a wide range of flow velocities.

The computed data on the influence of the angle of attack on the LTT onset in the boundary layer on the prolate spheroid are summarized in Fig. 12 for both Mach numbers ($M_\infty = 0.13$ and 0.7) with the use of the same threshold N factors N_{TS} and the N_{CF} computed by formula (2) with a corresponding degree of freestream turbulence Tu. The numerical data are approximated by the solid lines; the available experimental data [27] for $M_\infty = 0.13$ are also shown. It is seen that the Reynolds number of the LTT onset in the spheroid boundary layer monotonically decreases with an increase in the angle of attack on the upper surface, whereas the dependence on the angle of attack on the side surfaces is nonmonotonic. It should also be noted that the curves of the Reynolds number of the LTT onset on the spheroid for both flow regimes are quite similar to each other.

B. Transonic Flow at the Engine Nacelle

The transonic numerical simulations of the flow at the engine nacelle (Fig. 1d) are discussed in the following. As compared to
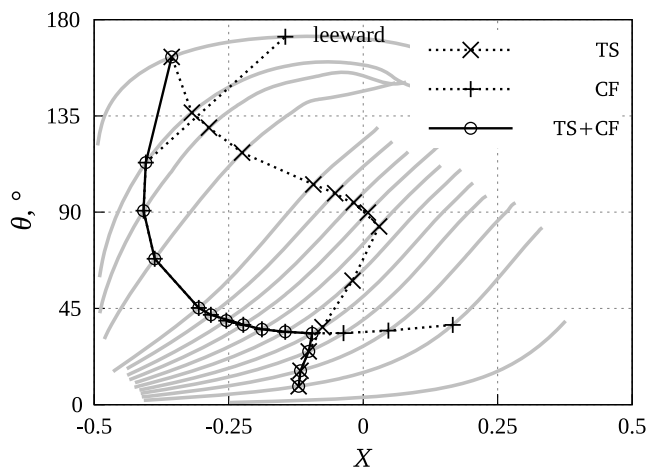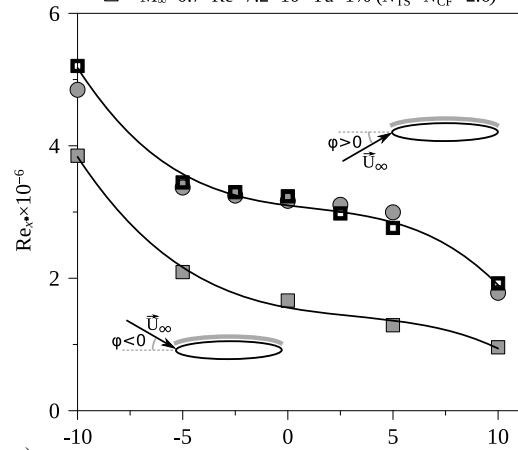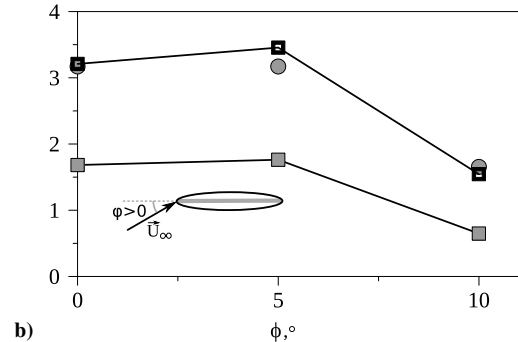
Fig. 10 Projections of streamlines onto the prolate spheroid surface and LTT onset position versus the azimuthal angle θ: $Re = 7.2 \times 10^6$, $M_\infty = 0.7$, Tu = 1% ($N_{TS} = N_{CF} = 2.6$), and $\varphi = +5$ deg.

Fig. 11 Projections of streamlines onto the prolate spheroid surface and LTT onset position versus the azimuthal angle θ: $Re = 7.2 \times 10^6$, $M_\infty = 0.7$, Tu = 1% ($N_{TS} = N_{CF} = 2.6$), and $\varphi = +10$ deg.

Fig. 12 Reynolds number of the LTT onset versus the angle of attack on the upper surface of the prolate spheroid at a) $Z = 0$ and b) on the side surface at $Y = 0$.

the spheroid considered earlier in this paper, the flow at the engine nacelle has some specific features (presence of a duct and the smaller length in the streamwise direction). The flow at the engine nacelle for the freestream Mach number of $M_\infty = 0.7$ has a supersonic region,
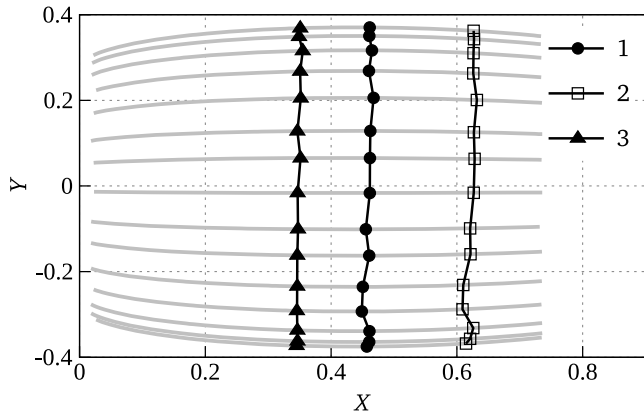

Fig. 13 Projections of streamlines onto engine nacelle surface ($\varphi = 0$) with indicated position of LTT onset (black curve): $Re = 4.2 \times 10^6$ and $M_\infty = 0.3$ (filled circles); $Re = 4.2 \times 10^6$ and $M_\infty = 0.7$ (open squares); and $Re = 10.38 \times 10^6$ and $M_\infty = 0.7$ (filled rectangles). Tu = 0.2% ($N_{TS} = 6.5$).
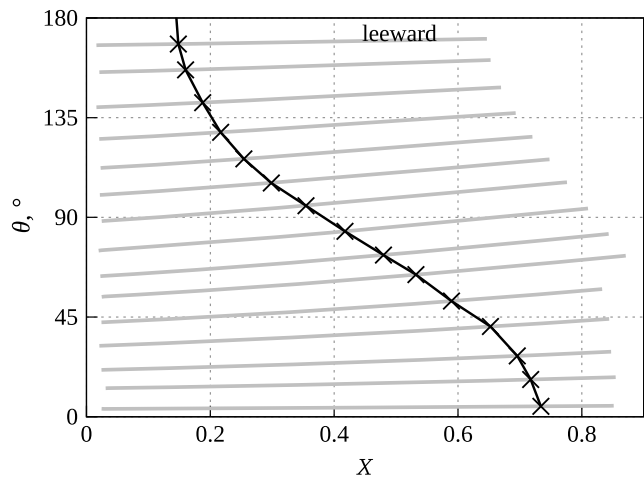

Fig. 14 Projections of streamlines onto the engine nacelle surface and LTT onset position versus the azimuthal angle θ: $Re = 10.38 \times 10^6$, $M_\infty = 0.7$, Tu = 0.2% ($N_{TS} = N_{CF} = 6.5$), and $\varphi = +5$ deg.
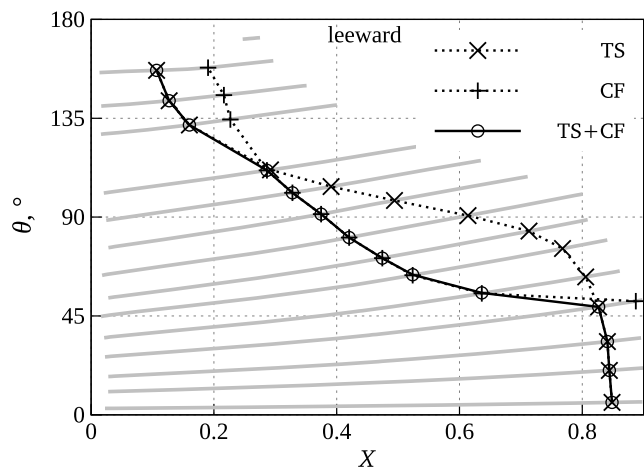

Fig. 15 Projections of streamlines onto the engine nacelle surface and LTT onset position versus the azimuthal angle θ: $Re = 10.38 \times 10^6$, $M_\infty = 0.7$, Tu = 0.2% ($N_{TS} = N_{CF} = 6.5$), and $\varphi = +10$ deg.

which distinguishes this transonic regime from the subsonic flow with an identical Reynolds number and freestream turbulence.

The LTT onset in the transonic flow at the engine nacelle was computed for Reynolds numbers of $Re = 4.2 \times 10^6$ and $Re = 10.38 \times 10^6$. For comparisons with the data obtained in the transonic flow regime, we also computed the LTT position in the engine nacelle boundary layer in the subsonic flow regime at $M_\infty = 0.3$ and $Re = 4.2 \times 10^6$. The comparison of the LTT positions in Fig. 13 for different regimes at a zero angle of attack shows that the onset of the transition in the engine nacelle boundary layer at a fixed Reynolds number is shifted in the downstream direction as the Mach number increases. Such dependence was also observed for the flat plate, airfoil, and prolate spheroid. An increase of the Reynolds number at a fixed Mach number leads to upstream shifting of the LTT position.

Figures 14 and 15 show the projections of streamlines onto the surface with the indicated position of LTT onset. The N-factors were computed by the LTT module for the boundary layer of the engine nacelle at the angles of attack of $\varphi = 5$ and 10 deg for $M_\infty = 0.7$,
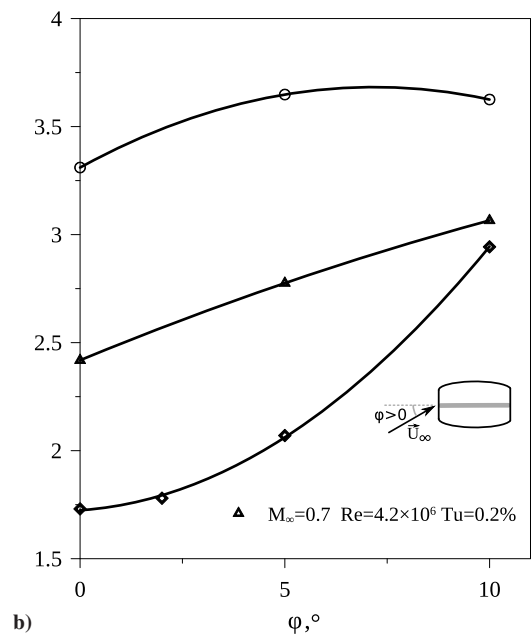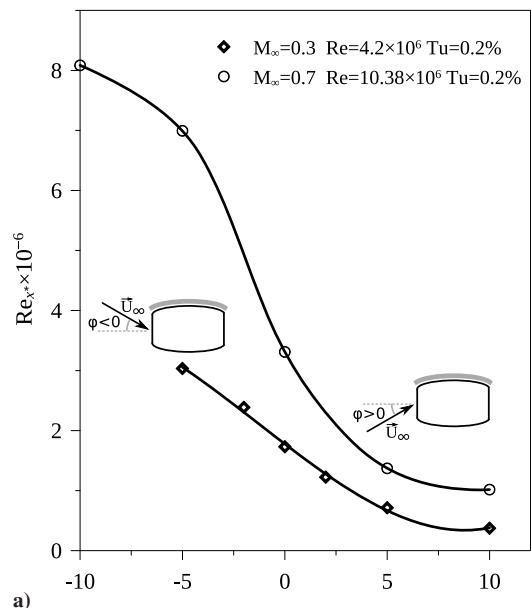

Fig. 16 Reynolds number of the LTT onset versus the angle of attack on the upper surface of the engine nacelle at a) $Z = 0$ and b) on the side surface at $Y = 0$.
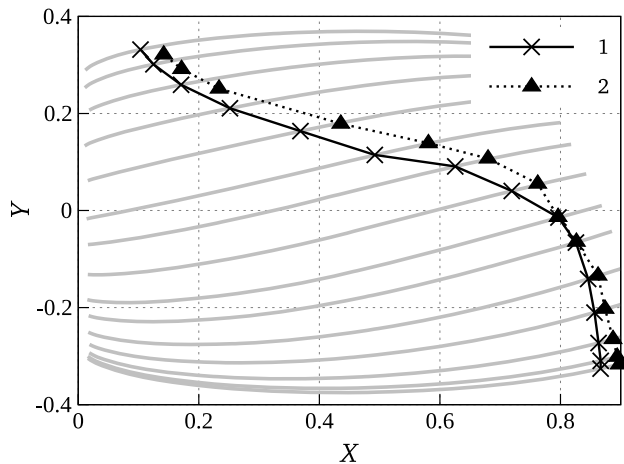
Fig. 17   Projections of streamlines onto the engine nacelle surface with the indicated LTT onset position (black curve): $M_\infty = 0.3$ (×) and $M_\infty = 0.7$ (filled rectangle). $Re = 4.2 \times 10^6$, $\varphi = +10$ deg, and $Tu = 0.2\%$ ($N_{TS} = 6.5$).

$Re = 10.38 \times 10^6$, and Tu = 0.2% (Nc = 6.58) for TS waves and CF vortices. The resulting LTT onsets are shown in Figs. 14 and 15 as functions of the azimuthal angle θ. The projections of streamlines onto the surface are also shown by the gray color. At $\varphi = 5$ deg, the dominating effect on the LTT is produced by the TS instability waves. At the angle of attack $\varphi = 10$ deg, the LTT is induced by the TS waves only near the windward and leeward surfaces, whereas the CF instability dominates on the major part of the near-wall flow. Thus, as the angle of attack increases, the role of the CF instability becomes more and more important in the case of the engine nacelle, which is similar to the case of the prolate spheroid.

Figure 16 shows the computed results on the influence of the angle of attack on the LTT onset in the boundary layer of transonic flow. It is seen that on both surfaces of the nacelle, the Reynolds numbers of the transition onset monotonically decrease with an increase in the angle of attack (Fig. 16a). These observations are consistent with the data for the prolate spheroid (see Fig. 12a).

Concerning the side surface of the engine nacelle (Fig. 16b), the dependences of the transition Reynolds number on the angle of attack at $Re = 10.38 \times 10^6$ and $M_\infty = 0.7$ are nonmonotonic. At $Re = 4.2 \times 10^6$, the transition Reynolds number increases with the angle of attack for both $M_\infty = 0.7$ and $M_\infty = 0.3$; that is in contrast with the results for the prolate spheroid. This can be clarified by considering Fig. 17, which shows the LTT onset on the projections of streamlines onto the engine nacelle surface at $Re = 4.2 \times 10^6$, as well as the angles of attack of $\varphi = 10$ deg for $M_\infty = 0.3$ and $M_\infty = 0.7$, respectively. Note that in this case, the LTT is initiated by the TS instability waves. In contrast, at $Re = 10.38 \times 10^6$, $\varphi = 10$ deg, and $M_\infty = 0.7$ (see Fig. 15), the dominating mechanism of the LTT at the side surface of the nacelle is the CF instability. Thus, the LTT mechanism significantly affects the dependence of the transition Reynolds number on the angle of attack, which is an increasing curve if the TS instability mechanism dominates and a decreasing curve if the CF instability plays the major role.

V.   Conclusions

The paper describes the technology of computing 3-D transonic laminar–turbulent flows at 3-D aerodynamic bodies with the use of the general-purpose CFD software ANSYS Fluent with the LTT module based on the LOTRAN 3 software package. The method of the LTT prediction in completely non-self-similar 3-D boundary layers was described. The LTT module was implemented as a plug-in system added to ANSYS Fluent. To the authors' knowledge, such an LTT module was integrated with the general-purpose CFD software ANSYS Fluent for the first time.

The positions of the LTT induced by the growth of the amplitudes of the TS waves and CF vortices were numerically simulated for strongly 3-D flows at the prolate spheroid and engine nacelle with different Mach numbers, Reynolds numbers, and angles of attack for low freestream turbulence. The results obtained in the present study are found to be in good agreement with available numerical and experimental data.

New data on the positions and dominating mechanisms of the LTT in boundary layers of the spheroid and engine nacelle in transonic flows were obtained. In particular, the role of two mechanisms of the transition to turbulence (evolution of traveling TS waves and stationary CF vortices) was considered. It was demonstrated that one of these mechanisms dominates in different regions of the flow around the prolate spheroid and the engine nacelle aligned at an angle of attack; the role of the CF instability becomes more pronounced as the angle of attack increases.

Beginning from $\varphi = 5$ deg for the prolate spheroid and from $\varphi = 10$ deg for the engine nacelle, the LTT near the windward and leeward sides of the bodies under consideration was still caused by the TS waves; whereas the CF instability dominates on the side surfaces. Thus, the competition of laminar-turbulent transition mechanisms significantly affects the dependence of the Reynolds number of the transition onset on the angle of attack: as the angle grows, the Reynolds number increases when TS waves dominate, and it decreases when CF vortices dominate.

References

[1] Boiko, A. V., Kirilovskiy, S. V., Maslov, A. A., and Poplavskaya, T. V., "Engineering Modeling of the Laminar–Turbulent Transition: Achievements and Problems (Review)," *Journal of Applied Mechanics and Technical Physics*, Vol. 56, No. 5, 2015, pp. 761–776.
https://doi.org/10.1134/S002189441505003X
[2] Boiko, A. V., Dovgal, A. V., Grek, G. R., and Kozlov, V. V., *Physics of Transitional Shear Flows*, Springer-Verlag, Berlin, 2012.
https://doi.org/10.1007/978-94-007-2498-3
[3] Van Ingen, J. L., "A Suggested Semi-Empirical Method for the Calculation of the Boundary Layer Transition Region," Delft Univ. of Technology TR VTH-74, Delft, The Netherlands, 1956.
[4] Smith, A. M. O., and Gamberoni, N., "Transition, Pressure Gradient and Stability Theory," Douglas Aircraft Company Rept. ES 26388, Santa Monica, CA, 1956.
[5] Fedorov, A., and Obraz, A., "A Hybrid LST-RANS Method for Modelling of Laminar-Turbulent Transition," *Proceedings of the 7th European Conference for Aeronautics and Space Sciences*, EUCASS, Rhode-St-Genese, Belgium, 2017, Paper 11.
https://doi.org/10.13009/EUCASS2017-353
[6] Malik, M. R., "COSAL: A Black-Box Compressible Stability Analysis Code for Transition Prediction in Three-Dimensional Boundary Layers," NASA CR-65925, 1982.
[7] Malik, M. R., "eMalik: A New Spatial Stability Analysis Program for Transition Prediction Using the eN Method," High Technology Corp. Rept. 9203, Hampton, VA, 1992.
[8] Malik, M. R., "Boundary-Layer Transition Prediction Toolkit," AIAA Paper 1997-1904, 1997.
https://doi.org/10.2514/6.1997-1904
[9] Chang, C.-L., "The Langley Stability and Transition Analysis Codes (LASTRAC): LST, Linear and Nonlinear PSE for 2D, Axisymmetric, and Infinite Swept Wing Boundary Layers," AIAA Paper 2003-0974, 2003.
https://doi.org/10.2514/6.2003-974
[10] Johnson, H., and Candler, G., "Hypersonic Boundary Layer Stability Analysis Using PSE-Chem," AIAA Paper 2005-5023, 2005.
https://doi.org/10.2514/6.2005-5023
[11] Krimmelbein, N., and Krumbein, A., "Automatic Transition Prediction for Three-Dimensional Configurations with Focus on Industrial Application," *Journal of Aircraft*, Vol. 48, No. 6, 2011, pp. 1878–1887.
https://doi.org/10.2514/1.C031230
[12] Langtry, R. B., and Menter, F. R., "Correlation-Based Transition Modeling for Unstructured Parallelized Computational Fluid Dynamics Codes," *AIAA Journal*, Vol. 47, No. 12, 2009, pp. 2894–2906.
https://doi.org/10.2514/1.42362

[13] Grabe, C., Shengyang, N., and Krumbein, A., "Transport Modeling for the Prediction of Crossflow Transition," *AIAA Journal*, Vol. 56, No. 8, 2018, pp. 3167–3178.
https://doi.org/10.2514/1.J056200

[14] Boiko, A. V., Nechepurenko, Y. M., Zhuchkov, R. N., and Kozelkov, A. S., "Laminar-Turbulent Transition Prediction Module for LOGOS Package," *Thermophysics and Aeromechanics*, Vol. 21, No. 2, 2014, pp. 191–210.
https://doi.org/10.1134/S0869864314020061

[15] Nechepurenko, Y. M., and Boiko, A. V., LOTRANxx Software Package for Computing the Position of the Laminar-Turbulent Transition in Boundary Layers of Viscous Incompressible Fluid Flows on Surfaces with Small Curvature, Software Package, Inst. of Numerical Mathematics SB RAS, Software Official Registration Certificate No. 2013660060, Federal Intellectual Property Service, Russia, 2013.

[16] Boiko, A. V., Demyanko, K. V., and Nechepurenko, Y. M., "On Computing the Location of Laminar–Turbulent Transition in Compressible Boundary Layers," *Russian Journal of Numerical Analysis and Mathematical Modelling*, Vol. 32, No. 1, 2017, pp. 1–12.
https://doi.org/10.1515/rnam-2017-0001

[17] Boiko, A. V., Demyanko, K. V., Inozemtsev, A. A., Kirilovskiy, S. V., Nechepurenko, Y. M., Paduchev, A. P., and Poplavskaya, T. V., "Determination of the Laminar-Turbulent Transition Location in Numerical Simulations of Subsonic and Transonic Flows Past a Flat Plate," *Thermophysics and Aeromechanics*, Vol. 26, No. 5, 2019, pp. 629–637.
https://doi.org/10.1134/S0869864319050019

[18] Kirilovskiy, S. V., Boiko, A. V., Demyanko, K. V., Nechepurenko, Y. M., Poplavskaya, T. V., and Sidorenko, A. A., "On Integrating the LOTRAN 3.0 Package into the ANSYS Fluent CFD Software," *AIP Conference Proceedings*, Vol. 2125, No. 1, 2019, Paper 030098.
https://doi.org/10.1063/1.5117480

[19] Poplavskaya, T. V., Boiko, A. V., Demyanko, K. V., Kirilovskiy, S. V., and Nechepurenko, Y. M., "Numerical Simulation of the Transition to Turbulence in Subsonic and Transonic Flows," *Journal of Physics: Conference Series*, Vol. 1359, No. 1, 2019, Paper 012068.
https://doi.org/10.1088/1742-6596/1359/1/012068

[20] Kirilovskiy, S. V., Boiko, A. V., Demyanko, K. V., Ivanov, A. V., Nechepurenko, Y. M., and Poplavskaya, T. V., "Numerical Simulation of the Laminar-Turbulent Transition on a Swept Wing in a Subsonic Flow," *Journal of Physics: Conference Series*, Vol. 1359, No. 1, 2019, Paper 012070.
https://doi.org/10.1088/1742-6596/1359/1/012070

[21] Langlois, M., Masson, C., Kafyeke, F., and Paraschivoiu, I., "Automated Method for Transition Prediction on Wings in Transonic Flows," *Journal of Aircraft*, Vol. 39, No. 3, 2002, pp. 460–468.
https://doi.org/10.2514/2.2951

[22] Arthur, M. T., Horton, H. P., and Mughal, M. S., "Modelling of Natural Transition in Properly Three-Dimensional Flows," AIAA Paper 2009-3556, 2009.
https://doi.org/10.2514/6.2009-3556

[23] Streit, T., Horstmann, K., Schrauf, G., Hein, S., Fey, U., Egami, Y., Perraud, J., El Din, I. S., Cella, U., and Quest, J., "Complementary Numerical and Experimental Data Analysis of the ETW Telfona Pathfinder Wing Transition Tests," AIAA Paper 2011-0881, 2011.
https://doi.org/10.2514/6.2011-881

[24] Radespiel, R., Horstmann, K. H., and Redeker, G., "Feasibility Study on the Design of a Laminar Flow Nacelle," *Journal of Aircraft*, Vol. 27, No. 11, 1990, pp. 959–965.
https://doi.org/10.2514/3.45966

[25] Baker, T. J., "Mesh Generation: Art or Science?" *Progress in Aerospace Sciences*, Vol. 41, No. 1, 2005, pp. 29–63.
https://doi.org/10.1016/j.paerosci.2005.02.002

[26] Haghiri, A. A., Fallahpour, N., Mani, M., and Tadjfar, M., "Experimental Study of Boundary Layer in Compressible Flow Using Hot Film Sensors Through Statistical and Qualitative Methods," *Journal of Mechanical Science and Technology*, Vol. 29, No. 11, 2015, pp. 4671–4679.
https://doi.org/10.1007/s12206-015-1013-1

[27] Meier, H. U., and H.-P. Kreplin "Experimental Investigation of the Boundary Layer Transition and Separation on a Body of Revolution," *Zeitschrift für Flugwissenschaften und Weltraumforschung*, Vol. 4, No. 2, 1980, pp. 65–71.

[28] Kreplin, H.-P., Vollmers, H., and Meier, H. U., "Measurements of the Wall Shear Stress on an Inclined Prolate Spheroid," *Zeitschrift für Flugwissenschaften und Weltraumforschung*, Vol. 6, No. 4, 1982, pp. 248–252.

[29] Kreplin, H. P., "Three-Dimensional Boundary Layer and Flow Field Data of an Inclined Prolate Spheroid," *Selection of Experimental Test Cases for the Validation of CFD Codes*, Vol. II, AGARD-AR-303, Neuilly-Sur-Seine, France, 1994, Test Case C2.

[30] Cebeci, T., and Stewartson, K., "On Stability and Transition in Three-Dimensional Flows," *AIAA Journal*, Vol. 18, No. 4, 1980, pp. 398–405.
https://doi.org/10.2514/3.50772

[31] Nayfeh, A. H., "Stability of Three-Dimensional Boundary Layers," *AIAA Journal*, Vol. 18, No. 4, 1980, pp. 406–416.
https://doi.org/10.2514/3.50773

[32] Mack, L. M., "Stability of Three-Dimensional Boundary Layers on Swept Wings at Transonic Speeds," *Symposium Transsonicum III*, edited by J. Zierep, and H. Oertel, Jr., Springer-Verlag, Berlin, 1989, pp. 209–223.
https://doi.org/10.1007/978-3-642-83584-1_18

[33] Cebeci, T., Chen, H. H., Arnal, D., and Huango, T. T., "Three-Dimensional Linear Stability Approach to Transition on Wings and Bodies of Revolution at Incidence," *AIAA Journal*, Vol. 29, No. 12, 1991, pp. 2077–2085.
https://doi.org/10.2514/3.10844

[34] Krumbein, A., "eN Transition Prediction for 3D Wing Configurations Using Database Methods and a Local, Linear Stability Code," *Aerospace Science and Technology*, Vol. 12, No. 8, 2008, pp. 592–598.
https://doi.org/10.1016/j.ast.2008.01.005

[35] Perraud, J., Arnal, D., Casalis, G., Archambaud, J.-P., and Donelli, R., "Automatic Transition Predictions Using Simplified Methods," *AIAA Journal*, Vol. 47, No. 11, 2009, pp. 2676–2684.
https://doi.org/10.2514/1.42990

[36] Hirschel, E. H., *Basics of Aerothermodynamics*, Springer-Verlag, Berlin, 2005, pp. 201–202.
https://doi.org/10.1007/b137734

[37] Gaponenko, V. R., Ivanov, A. V., and Kachanov, Y. S., "Experimental Study of a Swept-Wing Boundary-Layer Stability with Respect to Unsteady Disturbances," *Thermophysics and Aeromechanics*, Vol. 2, No. 4, 1995, pp. 287–312.

[38] Lees, L., "The Stability of the Laminar Boundary Layer in a Compressible Fluid," NACA Rept. 876, 1947, pp. 329–377.

[39] Mack, L. M., "On the Stability of the Boundary Layer on a Transonic Swept Wing," AIAA Paper 1979-0264, 1979.
https://doi.org/10.2514/6.1979-264

[40] Moore, F. K., "Three-Dimensional Boundary Layer Theory," *Advances in Applied Mechanics*, Vol. 4, 1956, pp. 159–224.
https://doi.org/10.1016/S0065-2156(08)70373-9

[41] Mack, L. M., "Boundary-Layer Linear Stability Theory," NATO AGARD Rept. 709: Special Course on Stability and Transition of Laminar Flow, Neuilly-Sur-Seine, France, 1984, pp. 3.1–3.81.

[42] Crouch, J. D., and Ng, L. L., "Variable N-Factor Method for Transition Prediction in Three-Dimensional Boundary Layers," *AIAA Journal*, Vol. 38, No. 2, 2000, pp. 211–216.
https://doi.org/10.2514/2.973

[43] Walker, G. J., "Transitional Flow on Axial Turbomachine Blading," *AIAA Journal*, Vol. 27, No. 5, 1989, pp. 595–602.
https://doi.org/10.2514/3.10150

[44] Mack, L. M., "Linear Stability Theory and the Problem of Supersonic Boundary-Layer Transition," *AIAA Journal*, Vol. 13, No 3, 1975, pp. 278–289.
https://doi.org/10.2514/3.49693

[45] Schubauer, G. B., and Klebanoff, P. S., "Contributions on the Mechanics of Boundary-Layer Transition," NACA TN 3489, 1955.

[46] Kreplin, H.P., Vollmers, H., and Meier, H.U., "Wall Shear Stress Measurements on an Inclined Prolate Spheroid in the ONERA F1 Wind Tunnel," German Aerospace Center, DFVLR-AVA Rept. IB 222-84 A 34, Göttingen, Germany, June 1985.

[47] Stock, H. W., "eN Transition Prediction in Three-Dimensional Boundary Layers on Inclined Prolate Spheroids," *AIAA Journal*, Vol. 44, No. 1, 2006, pp. 108–118.
https://doi.org/10.2514/1.16026

[48] Krimmelbein, N., Radespiel, R., and Nebel, C., "Numerical Aspects of Transition Prediction for Three-Dimensional Configurations," AIAA Paper 2005-4764, 2005.
https://doi.org/10.2514/6.2005-4764

[49] Krimmelbein, N., and Radespiel, R., "Transition Prediction for Three-Dimensional Flows Using Parallel Computation," *Computers and Fluids*, Vol. 38, No. 1, 2009, pp. 121–136.
https://doi.org/10.1016/j.compfluid.2008.01.004

[50] Bassom, A. P., and Hall, P., "On the Interaction of Stationary Crossflow Vortices and Tollmien–Schlichting Waves in the Boundary Layer on a Rotating Disc," *Proceedings of the Royal Society A*, Vol. 430, No. 1878, 1990, pp. 25–55.
https://doi.org/10.1098/rspa.1990.0079

[51] Kachanov, Y. S., and Tararykin, O. I., "The Development of 3-D Separated Flows and Their Influence on the Stability and Laminar-Turbulent Transition," *Separated Flows and Jets*, edited by V. V. Kozlov, and A. V. Dovgal, Springer-Verlag, Berlin, 1991, pp. 737–740. https://doi.org/10.1007/978-3-642-84447-8_91

[52] Redeker, G., Horstmann, K., Köster, H., Thiede, P., and Szodruch, J., "Design for a Natural Laminar Flow Glove for a Transport Aircraft," AIAA Paper 1990-3043, 1990, p. 10. https://doi.org/10.2514/6.1990-3043

[53] Arnal, D., Casalis, G., and Houdeville, R., "Practical Transition Prediction Methods: Subsonic and Transonic Flows," *Advances in Laminar–Turbulent Transition Modelling*, von Kármán Inst. Lecture Series, RTO-EN-AVT-151, 2008, pp. 7.1–7.34. https://doi.org/10.14339/RTO-EN-AVT-151

S. Fu
Associate Editor